Novel g-C_3N_4/BiOCl$_x$I$_{1-x}$ nanosheets with rich oxygen vacancies for enhanced photocatalytic degradation of organic contaminants under visible and simulated solar light

Xiaonan Hu, Yao Zhang, Boji Wang, Hongjing Li*, Wenbo Dong*

Shanghai Key Laboratory of Atmospheric Particle Pollution and Prevention, Department of Environmental Science & Engineering, Fudan University, Shanghai, 200433, China

ABSTRACT

A novel oxygen vacancy-rich g-C_3N_4/BiOCl$_x$I$_{1-x}$ heterostructure nanosheet (BCI-**CN**-P) is successfully prepared by a facile coprecipitation method with the assistance of surfactant polyvinylpyrrolidone (PVP) for enhanced photocatalytic degradation of organic contaminants. Field Emission Scanning Electron Microscope and Field Emission Transmission Electron Microscope detect the formation of heterostructure, while X-ray photoelectron spectroscopy and electron spin resonance demonstrate that the surface has rich oxygen vacancies. Under visible light irradiation, BCI-**CN**-P (g-C_3N_4/BiOCl$_x$I$_{1-x}$ with PVP) exhibits 100% photocatalytic degradation efficiency of colorless bisphenol A (BPA, $10\,\mathrm{mg\,L^{-1}}$) within 40 min, while CN (pure g-C_3N_4), BCI (pure BiOCl$_x$I$_{1-x}$), BC-**CN**-P (g-C_3N_4/BiOCl with PVP) show negligible decomposition ability, and BCI-CN (g-C_3N_4/BiOCl$_x$I$_{1-x}$ without PVP) displays 61.2% removal efficiency for BPA after 1 h. Similarly, BCI-**CN**-P shows outstanding photocatalytic performance under simulated solar light, and the apparent reaction rate constant for BPA degradation is $0.2245\,\mathrm{min^{-1}}$, which is around 89.1, 15.2, 5.6 and 18.6 times as that of CN, BCI, BCI-CN and BC-CN-P, respectively. Furthermore, the photocatalytic mechanism of BCI-CN-P is revealed, the introduction of iodine and PVP enhance the visible light absorption ability and the formation of rich oxygen vacancies, and the synergistic effect between the g-C_3N_4/BiOCl$_x$I$_{1-x}$ heterojunction and oxygen vacancies facilitates the effective separation and transfer of photogenerated electron-hole pairs. $O_2\cdot^-$ radicals and photogenerated holes are confirmed to be main active species to decompose organic pollutants continuously during photocatalytic degradation process. The BCI-**CN**-P catalyst is excellent and applicable in the broad pH range from 5.0 to 9.0. Also, BCI-**CN**-P presents outstanding mineralization capability and bio-friendliness for potential practical application.

1. Introduction

Water pollution has become crucial issues which exerts serious harmful effect on ecological environment and human health [1]. Photocatalytic technology has been considered to be an efficient and eco-friendly method to eliminate organic pollutants in wastewater. It is of significant importance to develop the high-efficiency and eco-friendly photocatalysts for practical application [2,3]. Semiconductor photocatalytic materials have attracted explosive attention to synthesize highly efficient photocatalysts [4]. Bismuth oxychloride (BiOCl) as one of semiconductors has special layered structures, can provide enough space to polarize the associated atoms and orbitals, and thereby form an internal static electric field between $[Bi_2O_2]^{2+}$ and $[Cl_2]^{2-}$, which promotes the generation and separation of photoinduced electron-hole pairs [5,6]. However, BiOCl possesses the shortcomings with large band gap (~ 3.4 eV), showing good activity only under ultraviolet light irradiation [7].

Various strategies have been explored to enhance the photocatalytic degradation ability of BiOCl under visible light irradiation [8–11]. It has been investigated that the formation of solid solution was favorable to tune the band gap, crystal structure and electronic field (Strategy I) [12]. Especially, BiOI with narrow band gap (~ 1.8 eV) has strong harvesting visible light property [13], and the solid solution BiOCl$_x$I$_{1-x}$ could effectively improve photocatalytic activity [14,15]. For instance, kim et al. reported that three dimensional (3D) BiOCl$_x$I$_{1-x}$ microspheres exhibited enhanced photocatalytic activities than pure BiOCl for methyl **orange** (MO) and Rhodamine B (RhB) degradation under visible light irradiation [16]. Our group also prepared BiOCl$_x$I$_{1-x}$ nanospheres with excellent degradation ability toward p-hydroxyphenylacetic acid under simulated solar light [17,18]. Besides, photocatalytic activities of BiOCl

have also been improved by coupling other excellent semiconductor photocatalysts to construct the heterojunctions (Strategy II) [19,20]. Recently, graphitic carbon nitride (g-C_3N_4) has received wide attentions as a kind of promising photocatalyst due to its low cost, high stability, non-toxicity and narrow band gap (~ 2.7 eV) [21–23]. For example, 2D and 3D BiOCl-g-C_3N_4 heterostructures have been respectively successfully fabricated by Liu et al. and Wang et al., which showed excellent visible light photocatalytic performance for MO degradation than bare BiOCl and g-C_3N_4 [24,25]. In addition, it has been demonstrated that oxygen vacancies could not only optimize the band structure, but also promote the separation and transfer of charge carrier, thus improving the photocatalytic activities (Strategy III) [26,27]. Cai et al. synthesized the BiOCl nanosheets with oxygen vacancies using xylitol as the surfactant for the enhancement photodegradation of RhB [28]. Zou et al also prepared oxygen vacancies-rich BiOCl nanosheets by the addition of dulcitol, which could degrade RhB effectively [29].

The combination of two strategies has been proved to further enhance the photocatalytic performance of BiOCl. Shi et al. successfully prepared the BiOCl$_x$Br$_{1-x}$/g-C_3N_4 hybrid (Strategy I + Strategy II), which exhibited superior photocatalytic activity of RhB than pure BiOCl$_x$Br$_{1-x}$ and g-C_3N_4 [30]. Wang et al. synthesized the abundant oxygen vacancy BiOBr$_x$I$_{1-x}$ (Strategy I + Strategy III) and BiOCl-g-C_3N_4 with the addition of surfactant polyvinylpyrrolidone (PVP) (Strategy II + Strategy III), which exhibited higher photocatalytic activity for the degradation of 4-chlorophenol [31,32]. However, these works mainly focused on the dye degradation and few paid attention to the elimination of non-dye colorless organic contaminants. Even though the degradation of colorless organic pollutants has been reported, the removal efficiencies of total organic carbon (TOC) were unsatisfactory or not discussed. Therefore, it is highly desirable to construct novel nanosheets with rich oxygen vacancies for enhanced photocatalytic degradation of organic contaminants, especially colorless organic pollutants. Meanwhile, the as-designed photocatalysts should present better mineralization capability and bio-friendliness for future application.

Herein, we have successfully designed oxygen vacancy-rich nanosheets-like g-C_3N_4/BiOCl$_x$I$_{1-x}$ heterostructures with a facile coprecipitation method. A series of characterizations were employed to analyze the microstructure, components, surface and optical properties. The photocatalytic performance was then evaluated to decompose model colorless pollutant bisphenol A (BPA) under visible and simulated solar light. The effect of various factors including the pH value, catalysts amounts, initial BPA concentration and inorganic ions on photocatalytic activity and the recyclability of the catalysts were investigated. The mineralization and biotoxicity experiments were also carried out. Furthermore, ESR measurements and typical scavenger experiments were conducted to determine the main reactive species in this system, and the possible photocatalytic mechanism of BPA degradation was proposed.

2. Experimental section

2.1. Materials

HPLC-grade methanol was obtained from CNW Technologies GmbH (Germany). All other chemical reagents used in this work were analytical reagent grade and without further purification. BPA was purchased from Tokyo Chemical Industry Co., Ltd. Other chemicals were all purchased from Sinopharm Chemical Reagent Company. Deionized (DI) water was utilized throughout the experiments.

2.2. Catalysts preparation

2.2.1. Synthesis of pure g-C_3N_4 and BiOCl$_x$I$_{1-x}$

Bulk g-C_3N_4 was synthesized by thermal polycondensation of melamine as precursor. Briefly, 2 g melamine powder was put into an alumina crucible with a cover and calcinated at 550 °C for 4 h with a ramping rate of 2.5 °C min^{-1} in a furnace under air condition. After cooling to ambient temperature, the samples were collected and grounded into powders. 400 mg as-obtained bulk g-C_3N_4 was dispersed in 200 mL DI water and sonicated for 4 h. The light yellow powder was rinsed several times by DI water and dried at 80 °C overnight for next-step usage. It was labeled as CN (pure C_3N_4).

BiOCl$_x$I$_{1-x}$ powders were synthesized by precipitation of bismuth nitrate pentahydrate (Bi(NO$_3$)$_2$·5H$_2$O) with ammonia (NH$_3$·H$_2$O). Typically, 5.82 g Bi(NO$_3$)$_2$·5H$_2$O was added into 25 mL glycerol and stirred for 30 min at 80 °C (bottle A). Based on our previous investigations [17], 0.67 g KCl and 0.50 g KI was dissolved in 100 mL DI water (bottle B). The solution in the bottle B was introduced dropwise to the bottle A during vigorous stirring at 80 °C. NH$_3$·H$_2$O was added to adjust the pH value to 9.0 in the system. Subsequently, the whole solution was continuously stirred at 80 °C for 1 h. The resultant powders were washed thoroughly and dried at 80 °C overnight. It was denoted as BCI (pure BiOCl$_x$I$_{1-x}$).

2.2.2. Preparation of oxygen vacancy-rich g-C_3N_4/BiOCl$_x$I$_{1-x}$ hybrid

The g-C_3N_4/BiOCl$_x$I$_{1-x}$ hybrid with rich oxygen vacancies was prepared with the help of surfactant. In details, 0.3 g aforementioned CN nanosheets were added into 25 mL DI water and sonicated for 30 min (bottle C). Afterwards, 5.82 g Bi(NO$_3$)$_2$·5H$_2$O, 0.5 g polyvinylpyrrolidone (PVP, K-30) and 25 mL glycerol were successively introduced into the bottle C at 80 °C. The mixture was vigorously stirred for 30 min. The subsequent procedure, which started from the addition of the KCl and KI mixed solution, was similar to the synthesis of BCI. The schematic illustration of preparation process for g-C_3N_4/BiOCl$_x$I$_{1-x}$-PVP hybrid in details was described in Fig. S1. The products were washed several times to neutral and to remove extra surfactant before drying. It was denoted BCI-CN-P (g-C_3N_4/BiOCl$_x$I$_{1-x}$ with PVP).

2.2.3. Preparation of oxygen vacancy-poor g-C_3N_4/BiOCl$_x$I$_{1-x}$ hybrid

For comparison, the preparation of g-C_3N_4/BiOCl$_x$I$_{1-x}$ hybrid with poor oxygen vacancies was prepared in a similar way without adding PVP. The as-obtained sample was labeled as BCI-CN (g-C_3N_4/BiOCl$_x$I$_{1-x}$ without PVP). As a control sample with poor light absorption capability, the g-C_3N_4/BiOCl nanosheets were similarly synthesized without the addition of KI, and denoted as BC-CN-P (g-C_3N_4/BiOCl with PVP).

2.3. Characterization

The morphologies, microstructures and elemental distribution were investigated with Field Emission Scanning Electron Microscope (FESEM, Nova NanoSem 450) and Field Emission Transmission Electron Microscope (FETEM, Tecnai G2 F20 S-Twin) equipped with high-resolution TEM (HRTEM) and energy dispersive spectroscopy (EDS). The crystal structure and phase composition of the as-prepared materials were observed by X-ray powder diffraction (XRD, D8 Discovery A 25) equipped with a Cu-Ka radiation operated at 40 mA and 40 kV at a scan range of 10 °C ~ 90 °C. The Zeta potential of the materials was recorded on a zeta potential analyzer (Zetasizer Nano ZS90, Malvern, UK). The Fourier transform infrared (FTIR) spectra were collected on a Nicolet Nexus 470. N$_2$ adsorption–desorption isotherms and specific pore parameters were obtained at −196 °C on a Quantachrome instrument (Autosorb IQ2, USA) by using the Brunauer-Emmett-Teller (BET) and Barrett-Joyner-Halenda (BJH) and Density Functional Theory (DFT) method. The X-ray photoelectron spectroscopy (XPS) were performed by employing an RBD upgraded PHI-5000C ESCA system with a monochromatic Mg Kα excitation source. All binding energies (BE) were calibrated with the C 1s line at 284.6 eV attributed to the surface adventitious carbon. Curve fitting and background correction were accomplished by using AugerScan 3.21 software. The UV–vis diffuse reflectance spectroscopy (UV–vis DRS) data were conducted on a double beam UV–vis spectrophotometer (UV-2600, Shimadzu

Corporation, Japan) with $BaSO_4$ as a reference. The steady-state photoluminescence (PL) spectra of the catalysts were recorded on a fluorescence spectrometer (Edinburgh, FLS1000) at an excitation wavelength of 315 nm. The photocurrent and electrochemical impedance spectroscopy (EIS) were performed on the CHI 1030B and Zahner Zennium PP211 (Germany) electrochemical workstation, respectively. The electrodes were prepared by dropwise adding a 10 μL slurry containing 10 mg samples, ethyl alcohol and 1 mL 0.5% Nafion onto the Indium-Tin Oxide (ITO) glass and then dried in air at room temperature. The light source was a 350 W Xenon lamp with a 420 nm cutoff. The electrolyte was 0.5 M Na_2SO_4 solution. Electron spin resonance (ESR) spectra were obtained on a Bruker spectrometer (JEOL, FA200) with 5,5-Dimethyl-1-pyrroline-*N*-oxide (DMPO) as the spin trapper.

2.4. Photocatalytic performance measurement

The photocatalytic performance of as-prepared five samples was evaluated by measuring the degradation of BPA and Rhodamine B (RhB) under visible and simulated solar light. Photocatalytic reaction was performed in the photochemical reactor (XPA-VII, Xujiang electromechanical plant, Nanjing, China), which equipped with a 500 W Xenon lamp combined with a 290 nm and 420 nm cut-off filter as simulated solar and visible light source, respectively. The temperature of the reactor was maintained at 25 °C ± 2 °C by circulating water. 30 mg catalysts were dispersed in the cylindrical quartz tube containing 50 mL, 10 mg L^{-1} BPA or RhB aqueous solution. During reaction process, the mixture was under constant magnetic stirring. Before irradiation, the suspension were stirred in the dark for 4 h to reach adsorption-desorption equilibrium. During the photocatalytic process, 1 mL of the suspension were taken out at fixed intervals and then the catalysts were filtered from the solution via 0.2 μm filter.

The concentration of remaining BPA was analyzed by high performance liquid chromatography (HPLC, UltiMate 3000, Dionex, USA) with an Athena C18-WP (4.6 mm * 250 mm, 5 μm) column and a UV detector operated at 280 nm. The column temperature was 40 °C, and the injection volume was 20 uL. The mobile phase used for HPLC analysis was a mixture of ultrapure water and methanol (30/70, v/v) at a flow rate of 0.8 mL min^{-1}. The variations of RhB concentration were determined at maximum absorbance of 553 nm using a UV–vis spectrophotometer (Scinco, S-3100). The total organic carbon (TOC) was detected by Analytik Jena AG (Germany, multi N/C UV HS/1) to estimate the mineralization degree. The intermediate products of BPA were detected by liquid chromatography–mass spectrometry (LC–MS, UPLC I-Class-Xevo G2-XS QTOF Agilent 7890B) operated with negative modes electrospray ionization in the *m/z* 100 – 1200. The toxicity equivalent quantity was evaluated on the microplate reader (BioTek, Synergy H1, Winooski, VT, USA) with an excitation wavelength at 570 nm [33]. The pH was adjusted by 0.1 M $HClO_4$ and 0.1 M NaOH solution. Solution pH was measured using a pH meter (INESA Scientific Instrument Co., Ltd, China).

3. Results and discussion

3.1. The characterization of the catalysts

3.1.1. Morphology and microstructure

The microscopic morphology of as-prepared CN, BCI, BCI-CN and BC-CN-P samples were characterized by FESEM, and the corresponding images were shown in Fig. 1. The CN sample had rough, chunky and aggregated sheet-like structure with a size of several micrometers (Fig. 1a). BCI and BCI-CN both consisted of similar regular microspheres (Fig. 1b and c). It implied that the introduction of CN could not obviously destroy the hierarchical structure of pristine BCI. As for BC-CN-P, it had the uniform nanosheets-like morphology (Figs. 1d and 2 a).

Fig. 2b,c displays the high-magnification of FESEM and FETEM images of BCI-CN-P. The sample exhibited thin nanosheets structure

with wrinkle-like shape and good dispersion. In contrast with pure CN, the CN in the hybrids was not very rough, suggesting efficient exfoliation toward CN during the facile preparation procedure. As illustrated in corresponding EDS mapping images (Fig. 2d-k and Fig. S2), it was evident that bismuth, oxygen, chlorine, iodine, carbon and nitrogen were uniformly distributed over the BCI-CN-P nanosheet. It also suggested that CN had been successfully incorporated into BCI, further demonstrating that surfactant PVP could also promote intimate interfacial contact and therefore form tight heterojunction between CN and BCI.

XRD analysis was performed to investigate the phase structures of the as-obtained samples. Fig. 3a displays the XRD patterns of CN, BCI, BCI-CN, BC-CN-P and BCI-CN-P. Two distinct diffraction peaks located at around 13° (weaker) and 27.4° (stronger) were ascribed to in-plane repeated tri-s-thiazine units and interlayer stacking reflection of graphitic-like crystal structures, which indexed to (100) and (002) planes, respectively [34]. These peaks were a typical character of CN (JCPDS No.87-1526). The dominant diffraction peaks of BCI, BCI-CN, BC-CN-P and BCI-CN-P were similar to the standard pattern of tetragonal BiOCl (JCPDS No.06-0249) [35]. It indicated that the coupled CN could not apparently influence the original lattice structure of BCI. The peaks of CN were not observed in the patterns of BCI-CN and BC-CN-P, which might be due to the relatively low amounts of CN in the systems. However, the patterns of BCI-CN-P appeared a new small peak at 27.9°, which was assigned to CN. The slight shifting for CN might be derived from the strong interaction between CN and BCI. It also confirmed that more CN was really introduced into BCI, and they were better combined together by means of surfactant PVP. Compared with that of BC-CN-P in Fig. S3, the diffraction peak of BCI-CN-P showed slight shift toward the lower angle, which was owing to the introduction of the larger ionic radial I$^-$ (I$^-$, 2.20 Å; Cl$^-$, 1.81 Å) [14]. The shift indicated that the $BiOCl_xI_{1-x}$ had been formed as solid solutions. No other impurities were detected in all above mentioned samples, suggesting the formation of high purity phases during the preparation procedure.

Due to the introduction of iodine, it was conceivable that the interlayer spacing increased according to the Bragg's law. Moreover, the oxygen vacancies could also expand the interlayer spacing [36]. As can be seen from Fig. 3b, the HRTEM image of BCI-CN-P exhibited obvious layered structure of BCI with larger interlayer spacing of 0.804 nm. Additionally, two distinct orderly lattice fringes with a d-spacing of 0.268 nm and 0.336 nm were observed, which respectively corresponded to (110) plane of $BiOCl_xI_{1-x}$ and (002) plane of g-C_3N_4 [37,38]. These observations agreed well with the above XRD results.

3.1.2. Surface properties

As displayed in Fig. 4a, the zeta potential of bare CN and BCI with the concentration of 0.6 g·L^{-1} in DI water (pH = 7.5) were measured to be -33.1 mV and + 39.3 mV, respectively. It revealed that negatively charged CN could be self-assembly combined with positively charged BCI by electrostatic interaction with vigorous stirring. The opposite charge was beneficial to the formation of heterostructure. BC-CN-P and BCI-CN-P exhibited lower zeta potential in contrast with BCI and BCI-CN. It implied that the introduction of PVP could further promote the combination of bismuth-based compounds and CN.

FTIR spectra of as-obtained BCI-CN, BC-CN-P and BCI-CN-P materials were shown in Fig. 4b. The characteristic peaks observed at 1200 cm^{-1} - 1600 cm^{-1} (the cyan area) and 810 cm^{-1} were ascribed to the C–N heterocycles and triazine units in the g-C_3N_4, respectively. In addition, the absorption peak at 550 cm^{-1} was assigned to the typical symmetric stretching vibrational Bi-O band [39]. The peaks about CN and BCI coexist in the composites, indicating the hybrids have been successfully synthesized.

The N_2 adsorption desorption isotherms of the as-obtained materials are depicted in Fig. 4c, and the corresponding textual parameters were summarized in Table 1. The BET specific surface area (S_{BET}) of bare CN and BCI were approximately 16.8 m^2/g and 78.6 m^2/g, respectively.
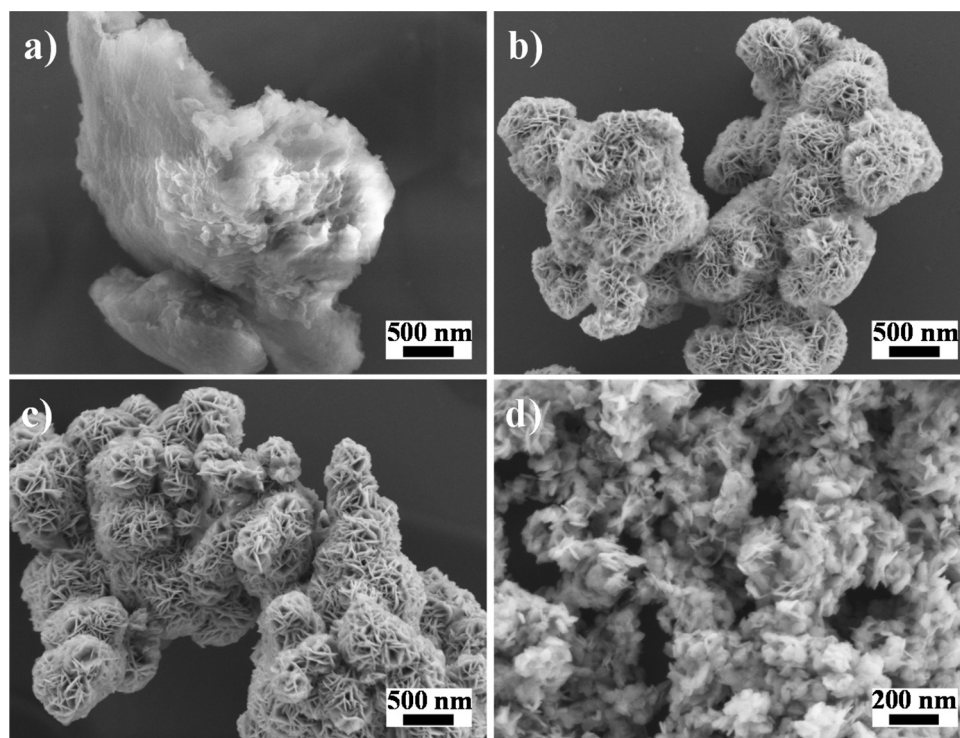
Fig. 1. FESEM images of CN (a), BCI (b), BCI-CN (c) and BC-CN-P (d).

While S_{BET} of hybrid BCI-CN, BC-CN-P and BCI-CN-P were respectively 27.9 m^2/g, 45.4 m^2/g and 72.3 m^2/g, which suggested that CN with lower S_{BET} was indeed incorporated into BCI and the hybrid had been successfully manufactured. It was found that S_{BET} of BC-CN-P and BCI-CN-P were higher than that of BCI-CN, further demonstrating the vital role of surfactant PVP for improving the S_{BET}. Notably, BCI-CN-P
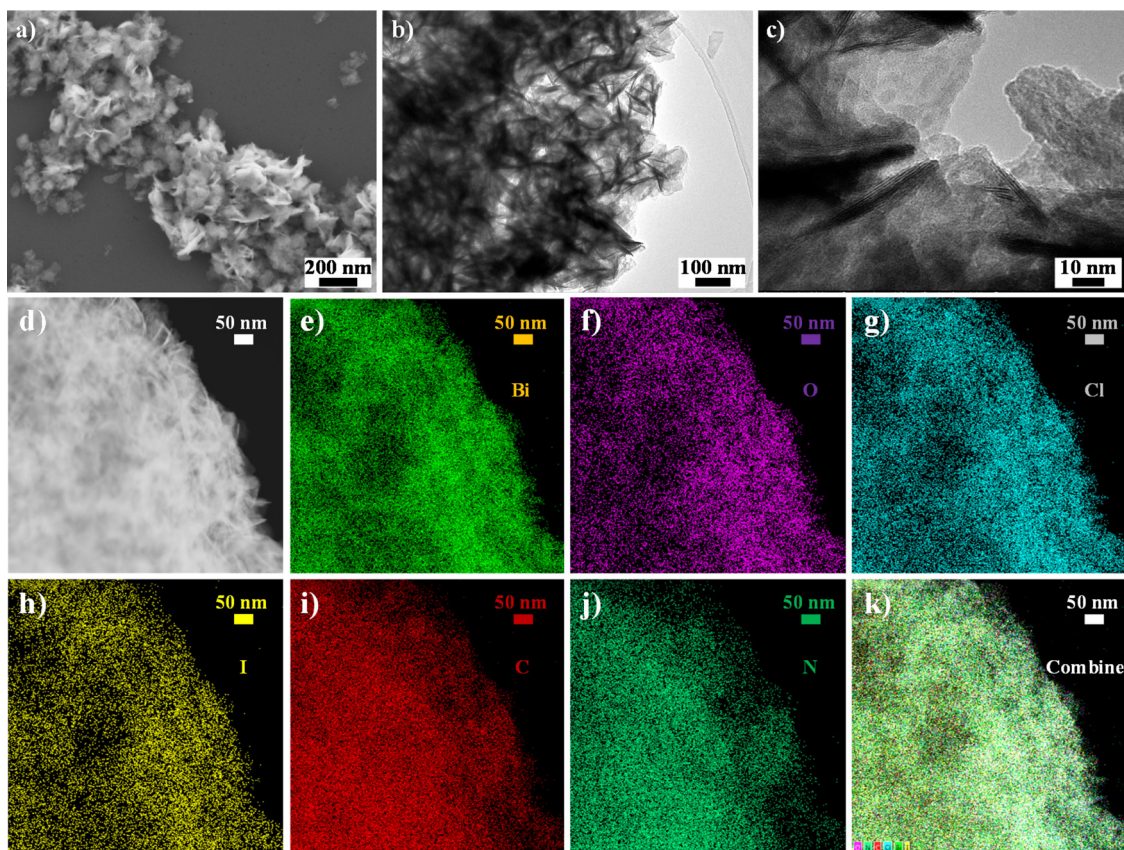

Fig. 2. FESEM (a) and FETEM images (b, c) of as-prepared BCI-CN-P; (d–k) EDS-mapping images of BCI-CN-P heterojunction.
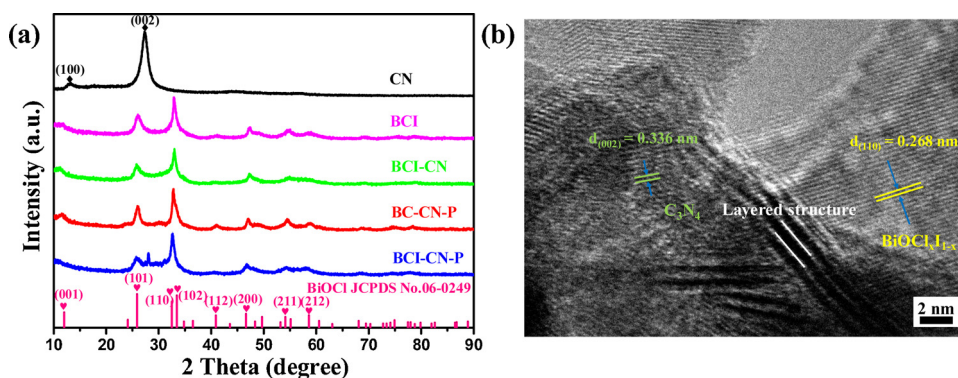
Fig. 3. (a) XRD patterns of as-prepared samples; (b) HRTEM image of BCI-CN-P heterojunction.

possessed higher S_{BET} and exhibited a classical type IV isotherm with a distinct H3 hysteresis loop observed at high pressures, implying the presence of slit-shaped mesopores. Moreover, the significant enhancement of S_{BET} and volume (0.24 cc/g) would tend to provide more abundant absorption or reactive activity sites, thus enhancing the photocatalytic activity [40].

XPS analysis was carried out to investigate the chemical composition and surface chemical state of the samples. As shown in Fig. 5a, the C 1s spectra of CN and BCI-CN-P both presented two peaks at 288.3 eV and 285.0 eV, which respectively corresponded to the sp^2 hybridized carbon (N−C═N) in the s-triazine rings and C−C bonds [41]. The binding energies for Bi 4f located at 164.2 and 158.9 eV were assigned to Bi $4f_{5/2}$ and Bi $4f_{7/2}$ of Bi^{3+} (Fig. 5b) [42]. Fig. 5c exhibits two main N 1s peaks of CN centered at 397.9 eV (N_1) and 399.6 eV (N_2), which were ascribed to the sp^2 hybridized nitrogen (C═N−C) in the s-triazine rings and bridging N of tertiary nitrogen in the form of N-C3 [25]. As for N 1s of BCI-CN-P, the N1 peak became weaker than that of CN, suggesting that the CN structure changed feebly by chemical interactions with the BCI to form the heterojunction. In Fig. 5d, the O1 s core XPS spectra could be deconvoluted into two peaks at 530.3 eV ($O_β$) and 531.4 eV ($O_α$), which were attributed to the lattice oxygen in the $[Bi_2O_2]^{2+}$ slabs and surface oxygen from oxygen vacancies [43,44]. The $O_α/ (O_α + O_β)$ ratio (59.3%) of BCI-CN-P was higher than that (34.4%) of BCI-CN, indicating that the introduction of surfactant PVP could enhance the formation of oxygen vacancies. The negatively charged −C═O bonds in surfactant PVP preferred to connect with the unsaturated positively charged Bi atoms on the $BiOCl_xI_{1-x}$ so as to lower the surface energy during the nucleation procedure, thus resulting in the formation of rich oxygen vacancies [45,46]. It was believed that the oxygen vacancies could act as electron capture center to facilitate the separation of photoinduced carriers and inhibit the recombination of photogenerated electron-hole pairs, thus significantly improving the photocatalytic activities [10,29,47,48]. Hence, BCI-CN-P with rich oxygen vacancies might be reasonably regarded as the high-efficiency photocatalyst.

Table 1
The physical properties of five as-obtained samples in details.

Samples	BET (m^2/g)	Pore Volume (cc/g)	Pore Diameter[a] (nm)
CN	16.8	0.06	1.4
BCI	78.6	0.11	4.0
BCI-CN	27.9	0.07	4.0
BC-CN-P	45.4	0.18	2.9
BCI-CN-P	72.3	0.24	3.2

[a] The pore diameter was computed from the desorption branch of the isotherm using the BJH (for mesopore) and DFT (for micropore) method.

3.2. Photocatalytic activity

3.2.1. Photocatalytic degradation of BPA

In order to evaluate the photocatalytic activity of the as-prepared samples under visible and simulated solar light, BPA was chosen as model non-dye colorless organic contaminant in the wastewater and thus the effect of dye-sensitization on photocatalytic performance could be eliminated. Moreover, BPA was a typical hazardous endocrine disrupter and hardly decomposed in the environment [15]. Before photocatalytic reaction, the adsorption-desorption equilibrium between BPA and samples was reached in the dark for 4 h (Fig. S4). Obviously, around 20% of BPA was adsorbed by BCI-CN-P after 1 h, and the adsorption of CN, BCI, BCI-CN and BC-CN-P on BPA was insignificant.

It can be seen from Fig. 6a that CN, BCI and BC-CN-P showed negligible photocatalytic decomposition ability for BPA under visible light irradiation. Blank experimental results indicated that the self-photolysis of BPA could be neglected, indicating that the structure of organic pollutant BPA was relatively stable. BCI-CN exhibited moderate photocatalytic activity and 61.2% of BPA was photodegraded after 1 h irradiation. Encouragingly, BCI-CN-P achieved the highest photocatalytic activity and BPA was completely degraded within 40 min. Similarly, under simulated solar sunlight, the order of photodegraded efficiency (Fig. 6c) was as follows: BCI-CN-P > BCI-CN > BCI > BC-CN-P > CN. Moreover, CN, BC-CN-P, BCI and BCI-CN all showed
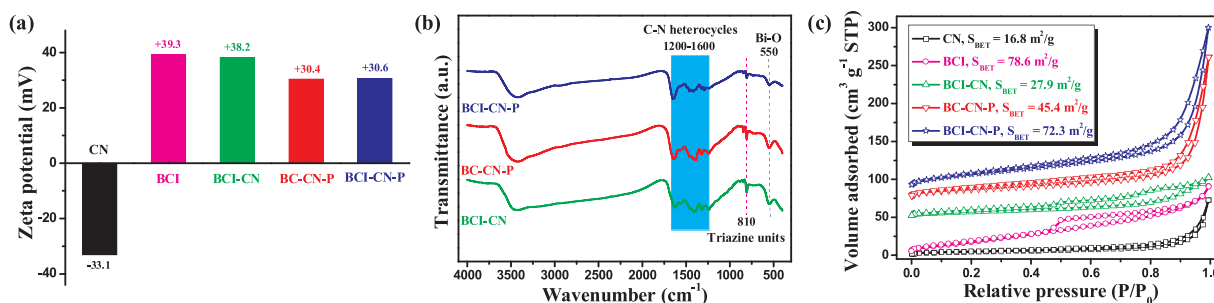

Fig. 4. Zeta potential in DI water (a), FTIR spectra (b) and nitrogen sorption isotherms (c) of as-obtained CN, BCI, BCI-CN, BC-CN-P and BCI-CN-P.
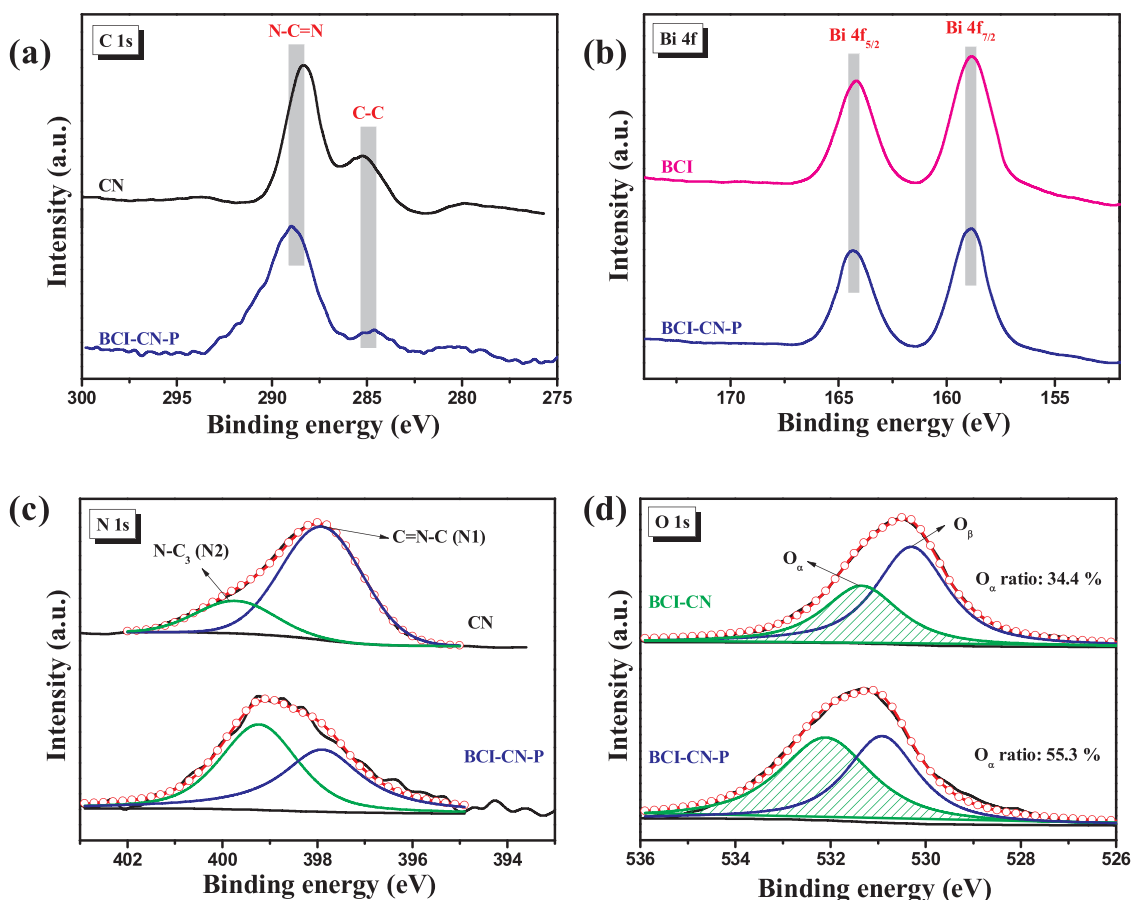
Fig. 5. XPS spectra of C 1s (a), Bi 4f (b), N 1s (c) and O 1s (d) for as-obtained samples.

nonnegligible removal efficiencies of BPA at 1 h, which were respectively 13.7%, 50.7%, 61.0% and 92.7%. Notably, BCI-CN-P presented optimal photocatalytic performance and 100% of BPA degradation efficiency was obtained within 30 min. As illustrated in Table S1, compared with the other g-C$_3$N$_4$-based photocatalysts reported in the literatures, BCI-CN-P catalysts displayed outstanding photodegradation performance toward BPA.

The photocatalytic degradation reaction obeyed Langmuir-Hinshelwood pseudo-first-order kinetics model (-ln(C/C$_0$) = kt). The plots of -ln(C/C$_0$) as a function of irradiation time and the corresponding apparent reaction rate constants (k value, the slope of the linear fitting curves) were described in Fig. 6b and d. In particular, BCI-CN-P showed outstanding photocatalytic performance under simulated solar light, and the apparent reaction rate constant of BPA degradation was 0.2245 min^{-1}, which was much higher than that of other samples (0.0025 min^{-1} for CN, 0.0148 min^{-1} for BCI, 0.0404 min^{-1} for BCI-CN, 0.0121 min^{-1} for BC-CN-P, respectively). Besides, it was about 1.94 times higher than that of BCI-CN-P (0.1160 min^{-1}) under visible light irradiation.

3.2.2. Mineralization capability and bio-friendliness

In order to evaluate the mineralization degree of BPA, TOC residual efficiencies (C/C$_o$) in the systems of five samples under visible and simulated solar light for 1 h were illustrated in Fig. 7a. The order of TOC residual efficiency under visible light irradiation was BCI-CN-P (21.9%) < BCI-CN (81.2%) < BCI (100%) ≈ BC-CN-P ≈ CN. Similarly, as-obtained samples presented higher photocatalytic performance under simulated solar sunlight, which was BCI-CN-P (12.2%) < BCI-CN (31.3%) < BCI (64.1%) < BC-CN-P (77.5%) < CN (89.7%). Fig. 7b figures out the change of TOC residual efficiency utilizing catalyst BCI-CN-P under visible or simulated solar light irradiation. The

concentration of TOC decreased quickly within 20 min. It suggested that BCI-CN-P not only significantly increased the degradation rate of BPA but also dramatically improved the mineralization degree, and the order of mineralization degree was in agreement with the sequence of removal efficiencies (Fig. S5). Moreover, the intermediate products of BPA degradation identified by LC–MS were illustrated in Table S2, the demethylation of BPA generated Item A with *m/z* of 199. Although low molecular weight organic acids were not detected by LC-MS, it could be inferred that the intermediates (such as Item B or C) would be further oxidized to low molecular weight organic acids and mineralized.

Toxicity equivalent quantity (TEQ) with respect to five catalysts under visible light irradiation for 1 h was measured to evaluate the biotoxicity, which was shown in the inset of Fig. 7c. As for catalysts BCI-CN and BCI-CN-P, the TEQ decreased by 31.6% and 67.6% after 1 h irradiation, respectively. However, TEQ was no obvious change of toward samples CN, BCI and BC-CN-P.

Apparently, BCI-CN-P presented outstanding mineralization capability and bio-friendliness. Therefore, the environmental influencing factors of BPA photocatalytic degradation with BCI-CN-P were investigated in order to evaluate the potential practical application.

3.2.3. The effect of pH

It was well-known that initial pH played a vital role in photocatalytic activity [49]. As shown in Fig. 8a, the influence of different initial pH (pH = 1.0, 3.0, 5.0, 7.5, 9.0 and 11.0) on the photocatalytic degradation of BPA was obvious. BPA could be totally removed in the range of initial pH 5.0 ~ pH 9.0 under visible light irradiation for 1 h. BCI-CN-P catalysts could photodegraded 70.7%, 92.1% and 86.7% of BPA at initial pH 1.0, 3.0 and 11.0, respectively. The initial pH 7.5 was found to be the optimum pH, which mainly exerted profound influence on the surface charge properties of photocatalysts [50]. Moreover, there
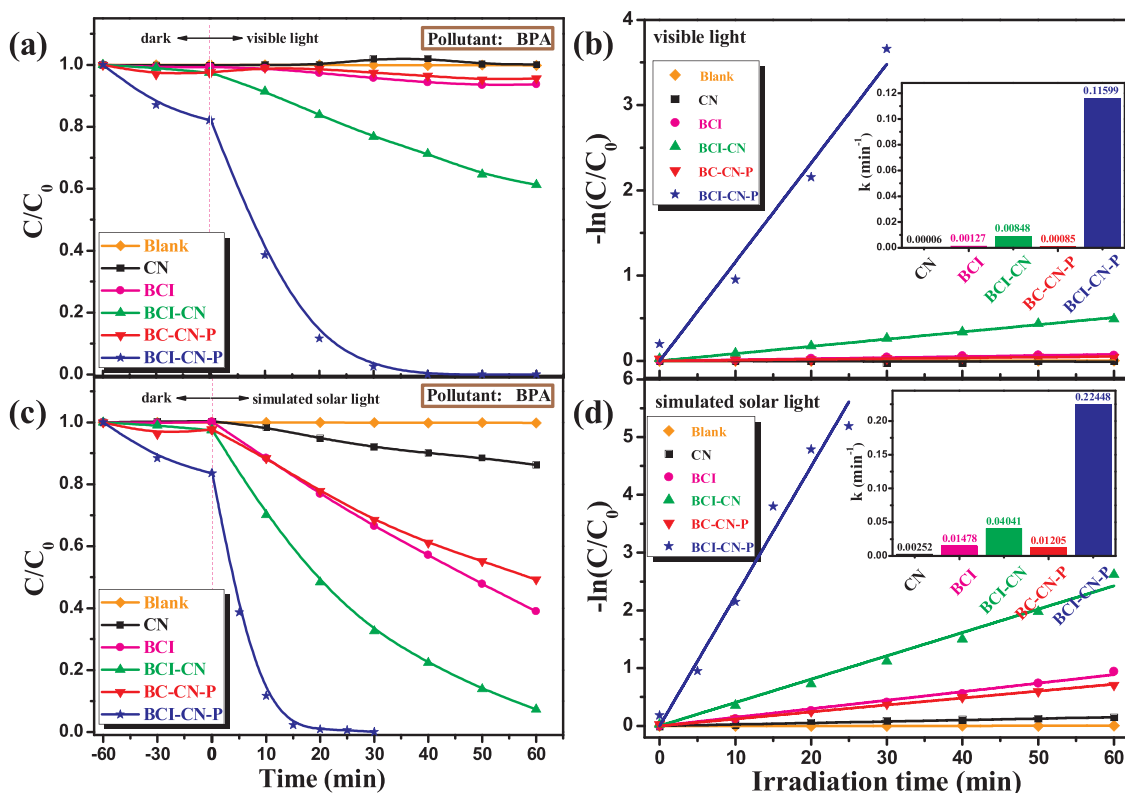
Fig. 6. Photocatalytic performance toward BPA removal under visible light irradiation (a) and simulated solar light (c) over five catalysts; Pseudo first-order kinetic fitting curves under visible light irradiation (b) and simulated solar light (d) over five catalysts; The insets of (b) and (d) were the corresponding apparent reaction rate constants (k).

Reaction conditions: [catalyst amounts] $= 0.6\,g \cdot L^{-1}$, [BPA concentration] $= 10\,mg \cdot L^{-1}$ and [solution volume] $= 50\,mL$.

was no remarkable change of pH during photocatalytic process while initial pH was 7.5, which illustrated in the inset of Fig. 8a. As seen from Fig. 8b, the surface charge properties gave a rise to a dramatical impact on the photocatalytic activity. The apparent reaction rate constants gradually increased with the increment of zeta potential at lower initial pH (pH ≤ 7.5). Vice versa the apparent reaction rate constants decreased at higher pH values (pH > 7.5) along with the decrement of zeta potential. It was concluded that BCI-CN-P catalyst was excellent and applicable in the broad pH range from 5.0 to 9.0 under visible light irradiation.

3.2.4. The effect of catalysts amounts and BPA concentration

The effect of BCI-CN-P catalyst amounts on BPA photocatalytic degradation was depicted in Fig. 8c. The BPA removal efficiency was apparently enhanced with the increase of the catalyst amounts from $0.2\,g \cdot L^{-1}$ to $0.6\,g \cdot L^{-1}$. However, furthermore increasing the catalyst

dosages from $0.6\,g \cdot L^{-1}$ to $1.0\,g \cdot L^{-1}$, the photocatalytic activities were slowly improved. Therefore, the BPA removal efficiency was also investigated by different initial BPA concentration with optimal catalyst dosages of $0.6\,g \cdot L^{-1}$ (Fig. 8d). The photocatalytic activity of BCI-CN-P decreased when the BPA concentration increased. Nonetheless, BCI-CN-P exhibited good photocatalytic performance in a wide BPA concentration range from $5\,g \cdot L^{-1}$ to $25\,g \cdot L^{-1}$.

3.2.5. The effect of inorganic ions

The influence of inorganic ions, including NO_3^-, $H_2PO_4^-$ and HCO_3^-, on the photocatalytic degradation of BPA was shown in Fig. 9. It can be concluded that NO_3^- with the concentration range of 0.1 mM~5 mM exerted no profound inhibition effect on photocatalytic performance (Fig. 9a). Generally, ·OH could be generated via the photolysis of NO_3^- [51], which implied that ·OH had little effect on BPA degradation. Fig. 9b-c shows that the photocatalytic activity was
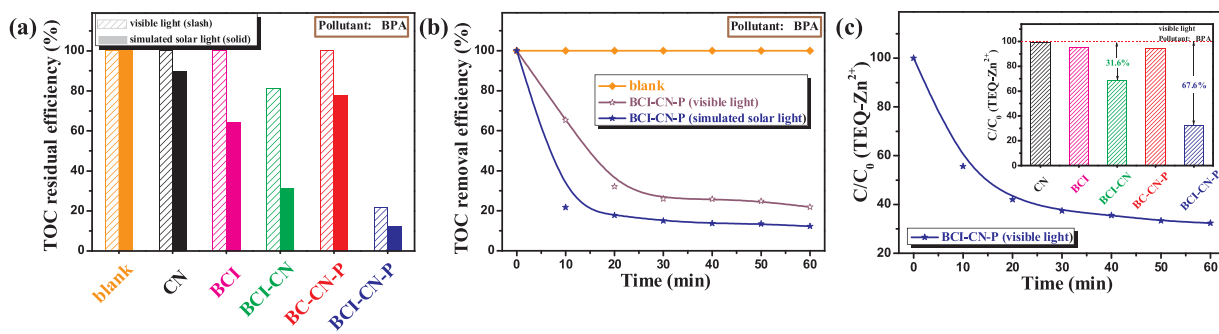

Fig. 7. (a) TOC residual efficiency for five photocatalysts toward BPA removal under visible and simulated solar light irradiation of 1 h; (b) The variations of TOC residual efficiency over BCI-CN-P catalysts with different light irradiation time; (c) The biotoxicity as a function of visible light irradiation time over BCI-CN-P catalysts; The inset of (c) was the biotoxicity over five photocatalysts after visible light irradiation of 1 h.
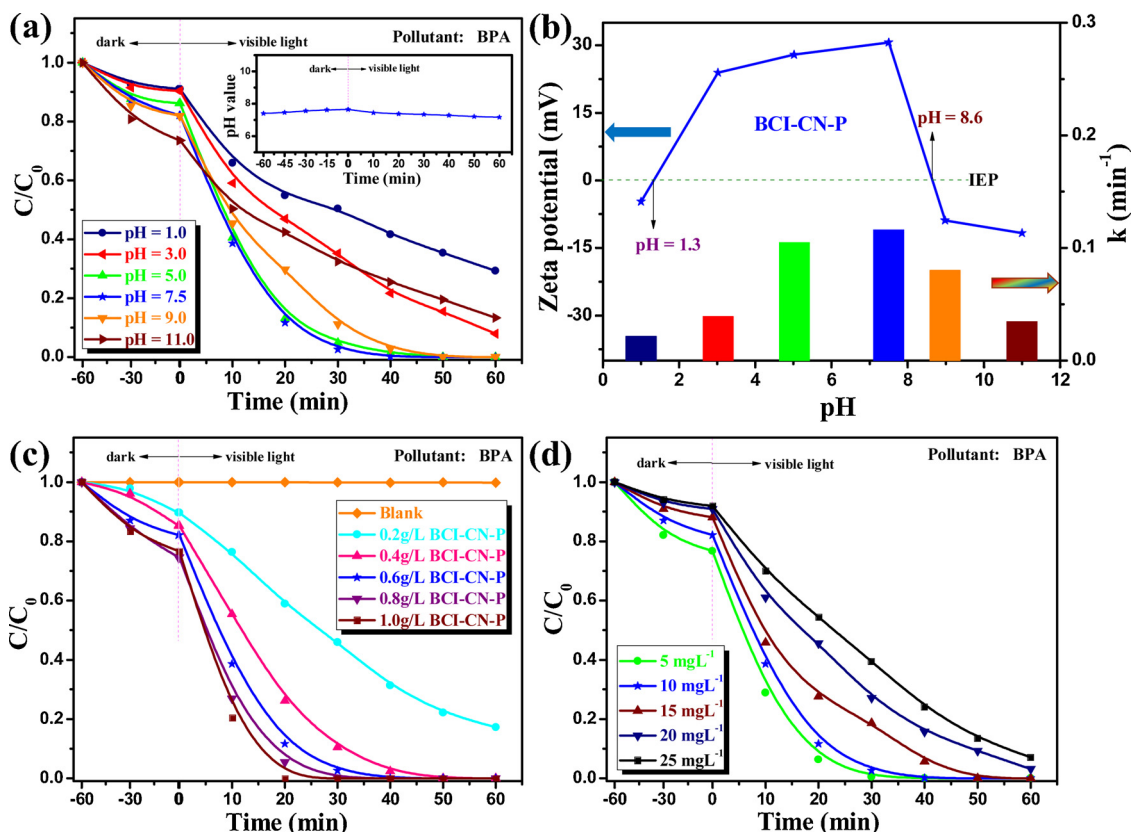
Fig. 8. (a) The effect of initial pH on the photocatalytic performance over BCI-CN-P toward BPA degradation; The inset of (a) The change of pH as a function of irradiation time at initial pH of 7.5; (b) The corresponding apparent reaction rate constants and zeta potential of BCI-CN-P at different initial pH in DI water; (c) The influence of catalysts amounts on the photocatalytic performance over BCI-CN-P toward BPA degradation; (d) The effect of BPA concentration on the photocatalytic performance over BCI-CN-P toward BPA degradation.
Reaction conditions: [catalyst amounts] $= 0.6\,g \cdot L^{-1}$, [RhB concentration] $= 10\,mg \cdot L^{-1}$, [solution volume] $= 50\,mL$.

decreased with the increase of $H_2PO_4^-$ or HCO_3^- concentration. Apparently, the adsorption capability of catalyst was restrained by the introduction of $H_2PO_4^-$ or HCO_3^- ions, which suggested that the decrease of photocatalytic activity might be due to the competition between inorganic ions $H_2PO_4^-$ or HCO_3^- and BPA molecules for active sites.

3.2.6. The recyclability of BCI-CN-P catalyst

The recyclability of the BCI-CN-P catalyst in the degradation of BPA has been evaluated (Fig. S6a). After four cycles of repeated use, BPA removal efficiency of 87.4% under visible light irradiation of 30 min was still achieved. The SEM and XRD analyses of BCI-CN-P catalyst after the recyclability test were illustrated in Fig. S6b, and the crystal structure and microscopic morphology of the BCI-CN-P catalysts exhibited negligible change before and after four cycles. These results suggested the good recyclability and structural stability of BCI-CN-P in

the photocatalytic degradation of BPA. These results suggested the good recyclability of BCI-CN-P in the photocatalytic degradation of BPA. Moreover, BCI-CN-P catalyst was used to degrade the dye colored RhB. Remarkably, under visible and simulated solar light, the BCI-CN-P catalyst exhibited the excellent photocatalytic activity with the rate constants of 0.05233 min^{-1} and 0.09455 min^{-1} (Fig. S7 and S8a), and the higher mineralization degree with 43.6% and 53.5% were obtained within 1 h (Fig. S8b).

3.3. Photocatalytic mechanism of BCI-CN-P catalyst

The adsorption capacity between pollutants and catalysts was believed to be an important factor for photocatalytic activity. To analyze the intrinsic photoreactivity, the normalized reactive activity (k/S_{BET}) was given in Fig. 10a. The normalized apparent rate constant of BCI-CN-P (1.6×10^{-3} g·m^{-2} min^{-1}) was much higher than that of CN, BCI,
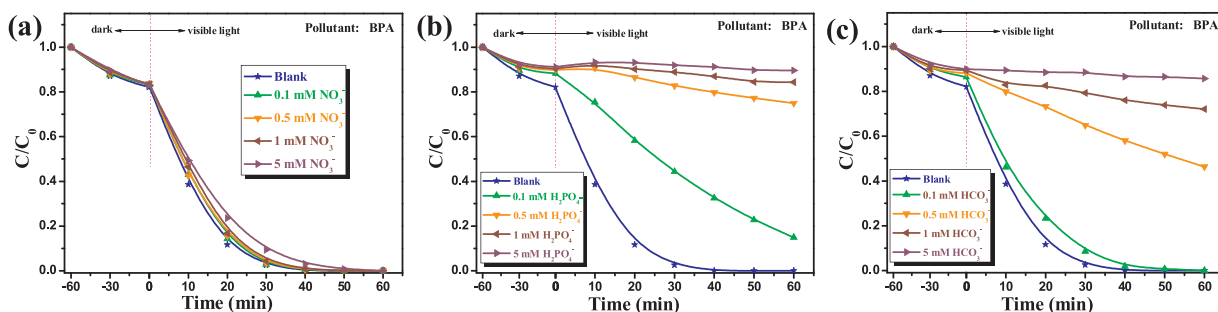

Fig. 9. The influence of NO_3^- (a), $H_2PO_4^-$ (b) and HCO_3^- (c) on the photocatalytic performance over BCI-CN-P toward BPA degradation.
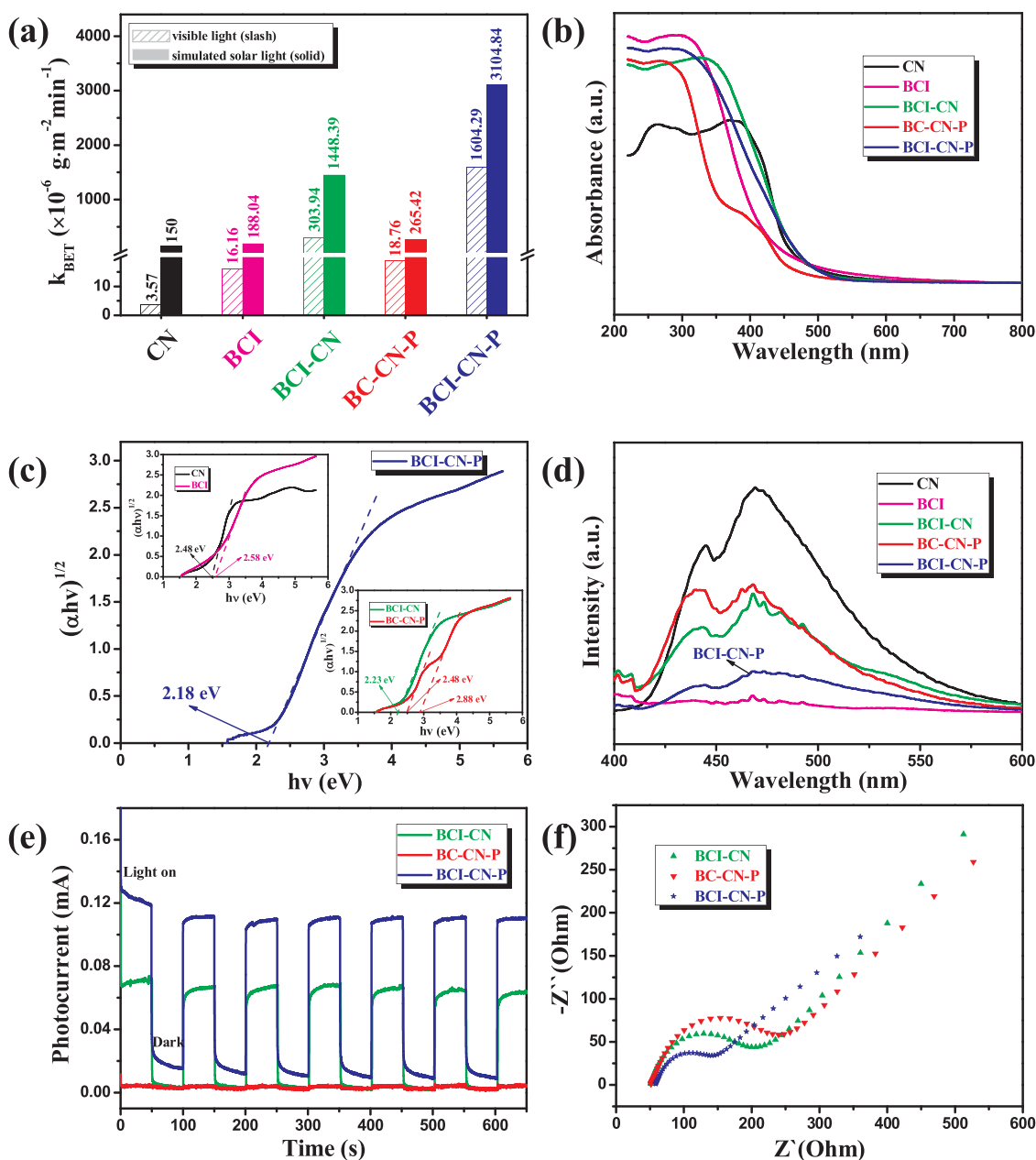
Fig. 10. (a) The normalized apparent reaction rate constants under different light irradiation; (b) UV–vis DRS spectra of different photocatalysts; (c) Plot of the $(\alpha h\nu)^{1/2}$ photon versus $h\nu$ for the band gap energy; (d) PL spectra of five photocatalysts; Transient photocurrent responses (e) and electrochemical impedance spectra (f) of the samples under visible light irradiation (wavelength > 420 nm).

BCI-CN and BC-CN-P under visible light irradiation. Besides, BCI-CN-P also exhibited higher normalized apparent rare constant (3.1×10^{-3} g·m^{-2} min^{-1}) under simulated solar light. It suggested that the surface area was not a predominant element affecting the photocatalytic activity in our study.

Fig. 10b depicted UV–vis DRS spectra of the as-obtained samples. Pure CN and BCI showed the typical absorption edge at 500 nm and 481 nm, respectively. The hybrids exhibited obvious red-shifts compared with bare BCI and CN. It indicated that the coupled BCI with CN could greatly improve the light harvesting ability. Two distinct absorption edges of BC-CN-P at about 500 nm and 431 nm were ascribed to the feature of CN and BC, respectively. It meant that the heterojunction in BC-CN-P was not well formed. BCI-CN-P presented considerable visible light absorption capacity with absorption edge of 569 nm. The photoabsorption ability of the BCI-CN-P was better than that of the BC-CN-P, implying that the incorporated iodine was

beneficial to the increment of light harvesting. It was well-known that the red-shifting of absorption edge usually meant the narrowing of band gap [52]. The plots of $(\alpha h\nu)^{1/2}$ versus $h\nu$ by the Kubelk-Munk method were described to further research the band structure of five catalysts (Fig. 10c). The values of band gaps for CN, BCI and BCI-CN were respectively estimated to be 2.48 eV, 2.58 eV and 2.23 eV, while BC-CN-P exhibited two band gaps at 2.48 eV and 2.88 eV. Notably, BCI-CN-P showed the narrowest band gap at 2.18 eV. Thus, stronger visible light harvesting ability and narrower band gap for BCI-CN-P were both conducive to the enhancement of photocatalytic performance.

To investigate the photocatalytic quantum efficiencies and photogenerated charge transport process, the PL emission spectra of five catalysts were given in Fig. 10d. Generally, lower PL intensity implied lower recombination of photoexcited electrons and holes, endowing higher photocatalytic activity [53]. CN showed a strong PL peak, indicating that more photoexcited electrons and holes were formed and
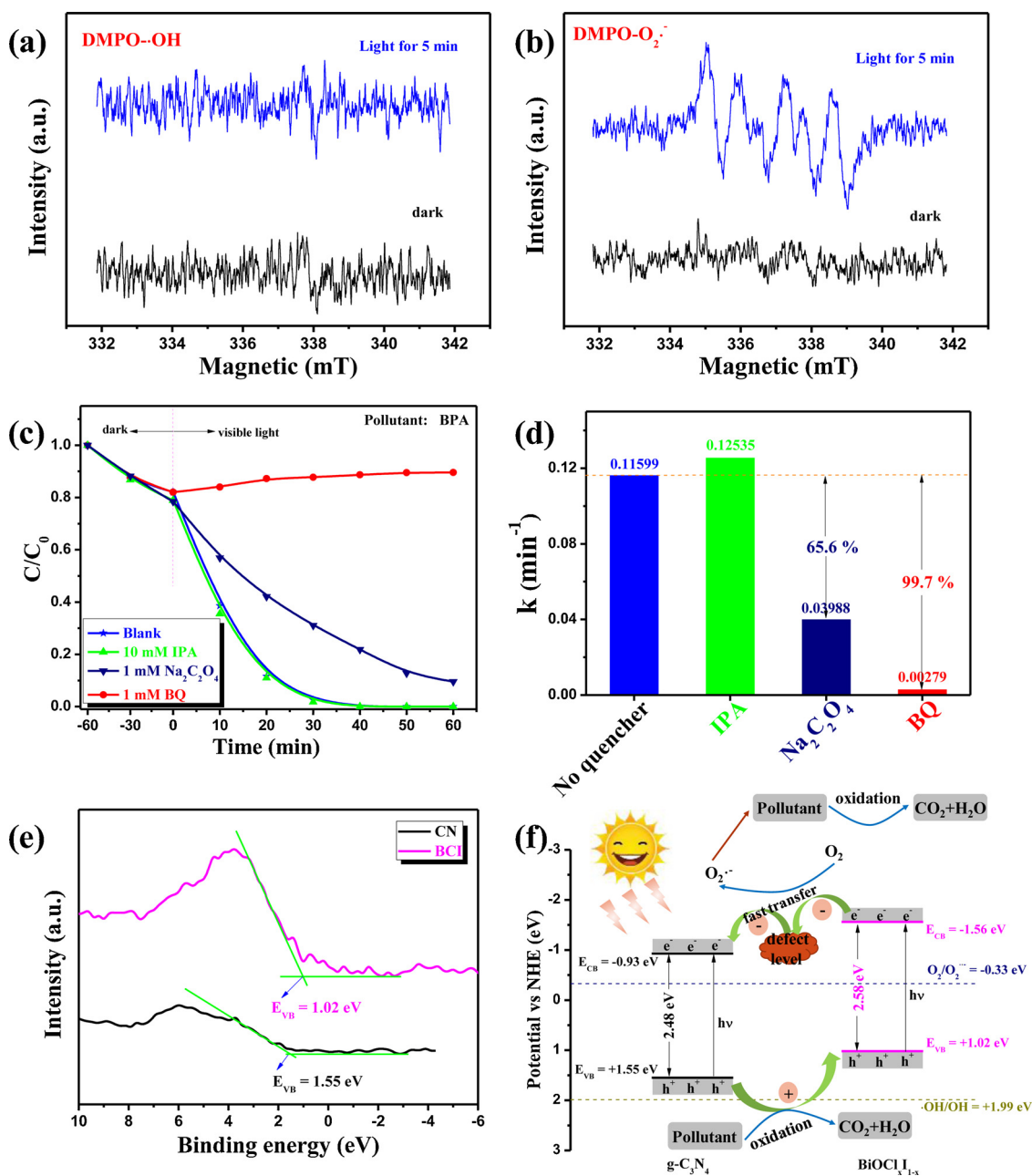
Fig. 11. The ESR spectra of DMPO-·OH (a) and DMPO-O$_2$·$^-$ (b) using BCI-CN-P in the dark and under visible light irradiation; (c) The photocatalytic performance over BCI-CN-P toward BPA degradation in the presence of different scavengers under visible light irradiation; (d) The corresponding apparent reaction rate constants with different scavengers; (e) VB-XPS spectra of CN and BCI; (f) Schematic illustration of energy band structures and electron-hole pairs separation over BCI-CN-P nanosheets.

recombined rapidly. While the intensity of fluorescence emission peak for BCI was the lowest, suggesting that fewer photoinduced electron hole pairs were generated on BCI, thus leading to the poor photocatalytic activity. However, BCI-CN-P exhibited lower PL peak, revealing that BCI-CN-P could efficiently promote the transportation and suppress the recombination of charge carriers.

The transient photocurrent response of various prepared catalysts is displayed in Fig. 10e. Compared to BCI-CN and BC-CN-P, BCI-CN-P composites displayed stronger photocurrent intensity under visible light irradiation, which indicated that BCI-CN-P catalysts had higher separation efficiency and longer lifetime of the photoinduced carriers. Subsequently, EIS experiments were conducted to further explore the mobility and separation efficiency of photogenerated carriers. As shown in Fig. 10f, the impedance of BCI-CN-P was much lower than that of

BCI-CN and BC-CN-P, which was testified by the smaller arc radius in the EIS Nyquist plots, suggesting that faster transfer of the carriers was occurred [54]. These data were well consistent with the PL results.

ESR measurements and typical scavenger experiments were carried out to assess the contribution of the main oxidative species to the photocatalytic degradation of BPA. As shown is Fig. 11a and b, the negligible signals for DMPO-OH adduct were detected after visible light irradiation of 5 min, while the strong ESR peaks with the relative intensity ratio of 1:1:1:1 corresponding to DMPO-O$_2$·$^-$ adduct were distinctly observed [55]. Besides, no obvious ESR signals of DMPO-OH and DMPO-O$_2$·$^-$ adduct were obtained in the dark. ESR spectra of as-obtained BCI-CN-P was also shown in Fig. S9, suggesting that the surface of the BCI-CN-P catalyst had rich oxygen vacancies [56], which was well matched with the XPS analysis. These results confirmed that O$_2$·-

radical was generated in the photodegradation process over BCI-CN-P catalyst.

The presence of glycerol was important to act as reducing agent favoring the formation of oxygen vacancies [57], however, the introduction of PVP could further increase the concentration of oxygen vacancies, which was evidenced by ESR results in Fig. S9. Compared with BCI-CN catalyst, BC-C**N**-P and BCI-C**N**-P catalysts exhibited stronger ESR signal intensities. Furthermore, as illustrated in Fig. 11c,d, the photodegradation activity of BCI-C**N**-P showed negligible variation after adding the isopropanol (IPA, hydroxyl radical scavenger). However, the degradation efficiencies of BPA decreased from 100% to 34.4% and 0.3% in the presence of $Na_2C_2O_4$ (hole scavenger) and 1, 4-Benzoquinone (BQ, superoxide radical scavenger), respectively. These results demonstrated that $O_2^{\cdot-}$ and h^+ were the dominant active species in the photocatalytic process, while OH radicals had almost no contribution to BPA removal.

The valence band (VB) edge positions of g-C_3N_4 and $BiOCl_xI_{1-x}$ were investigated by the VB-XPS to further analyze the photoinduced electron-hole pairs' separation mechanism. It can be calculated from Fig. 11e that the VB positions of CN and BCI were at 1.55 eV and 1.02 eV, respectively. Based on the band gaps, the conduction band (CB) edges of CN and BCI were estimated to be -0.93 eV and -1.56 eV according to the equation ($E_{CB} = E_{VB} - E_g$). It suggested that the heterojunction could be constructed between g-C_3N_4 and $BiOCl_xI_{1-x}$ due to the suitable band structures, which was beneficial to the separation of electron-hole pairs.

As illustrated in Fig. 11f, the pairs of electrons (e–) and holes (h^+) were photogenerated on the surface of g-C_3N_4 and $BiOCl_xI_{1-x}$ under visible light irradiation. Due to the influence by the effect of heterojunction and oxygen vacancies, e– in the CB of $BiOCl_xI_{1-x}$ first transferred to the defect level induced by oxygen vacancies, and then transferred to the higher CB of g-C_3N_4. The CB potentials of g-C_3N_4 and $BiOCl_xI_{1-x}$ were both lower than that of $O_2/O_2^{\cdot-}$ (-0.33 eV vs NHE), which permitted the generation of $O_2^{\cdot-}$ radicals via the reduction of dissolved O_2 by e–, thus $O_2^{\cdot-}$ could degrade organic pollutants constantly [58]. Meanwhile, h^+ in the VB of g-C_3N_4 transferred to the lower VB of $BiOCl_xI_{1-x}$, which was affected by the effect of heterojunction. The h^+ could not directly oxidize OH- into ·OH radicals because the VB potentials of g-C_3N_4 and $BiOCl_xI_{1-x}$ were both lower than that of OH-/·OH (+1.99 eV vs NHE), but h^+ could decompose organic pollutants continuously [59].

The introduction of iodine and PVP enhanced the visible light harvesting ability and the formation of rich oxygen vacancies, and the synergistic effect between the g-C_3N_4/$BiOCl_xI_{1-x}$ heterojunction and oxygen vacancies facilitated the effective separation and transfer of photogenerated electron-hole pairs. Therefore, the photocatalytic reaction was accelerated.

4. Conclusions

In this study, the novel oxygen vacancy-rich g-C_3N_4/$BiOCl_xI_{1-x}$ heterojunction with excellent photocatalytic activity was successfully fabricated with the assistance of surfactant PVP. FESEM and EFTEM detected the formation of heterostructure between $BiOCl_xI_{1-x}$ and g-C_3N_4, while XPS and ESR demonstrated that the surface had rich oxygen vacancies. Furthermore, the synergistic effect between heterojunction and oxygen vacancies ensured high-efficient separation and transfer of photoinduced charge carriers. Accordingly, the photocatalytic reaction was accelerated. BCI-C**N**-P showed 100% photocatalytic degradation efficiency of BPA (10 mg L^{-1}) within 40 min under visible light irradiation, while CN, BCI, BC-CN-P exhibited negligible decomposition ability, and BCI-CN displayed 61.2% removal efficiency for BPA after 1 h. Similarly, BCI-CN-P displayed the outstanding photocatalytic activity toward BPA degradation under simulated solar light with the apparent reaction rate constant of 0.2245 min^{-1}, which was about 89.1, 15.2, 5.6 and 18.6 times as that

of CN, BCI, BCI-CN and BC-CN-P, respectively. In addition, BCI-CN-P catalyst was excellent and applicable in the broad pH range from 5.0 to 9.0, it also presented outstanding mineralization capability and bio-friendliness, and higher BPA removal efficiency was still achieved after four cycles. This work prepared a novel photocatalyst with the introduction of iodine and PVP to enhance photocatalytic degradation of organic pollutants in environmental remediation.

Appendix A. Supplementary data

Supplementary material related to this article can be found, in the online version, at doi:https://doi.org/10.1016/j.apcatb.2019.117789.

References

[1] R.P. Schwarzenbach, T. Egli, T.B. Hofstetter, U. von Gunten, B. Wehrli, Global water pollution and human health, Annu. Rev. Env. Resour. 35 (2010) 109–136.

[2] S.T.M. Michael, R. Hoffmann, W. Choi, D.W. Bahnemann, Environmental applications of semiconductor photocatalysis, Chem. Rev. 95 (1995) 69–96.

[3] F. Fresno, R. Portela, S. Suárez, J.M. Coronado, Photocatalytic materials: recent achievements and near future trends, J. Mater. Chem. A Mater. Energy Sustain. 2 (2014) 2863–2884.

[4] J. Li, Y. Yu, L. Zhang, Bismuth oxyhalide nanomaterials: layered structures meet photocatalysis, Nanoscale 6 (2014) 8473–8488.

[5] Q. Li, X. Zhao, J. Yang, C.J. Jia, Z. Jin, W. Fan, Exploring the effects of nanocrystal facet orientations in g-C₃N₄/BiOCl heterostructures on photocatalytic performance, Nanoscale 7 (2015) 18971–18983.

[6] H. Gnayem, Y. Sasson, Hierarchical nanostructured 3D flowerlike BiOClₓBr₁₋ₓ semiconductors with exceptional visible light photocatalytic activity, ACS Catal. 3 (2013) 186–191.

[7] K. Zhang, C. Liu, F. Huang, C. Zheng, W. Wang, Study of the electronic structure and photocatalytic activity of the BiOCl photocatalyst, Appl. Catal. B: Environ. 68 (2006) 125–129.

[8] C.Y. Wang, Y.J. Zhang, W.K. Wang, D.N. Pei, G.X. Huang, J.J. Chen, X. Zhang, H.Q. Yu, Enhanced photocatalytic degradation of bisphenol A by Co-doped BiOCl nanosheets under visible light irradiation, Appl. Catal. B: Environ. 221 (2018) 320–328.

[9] F. Teng, W. Ouyang, Y. Li, L. Zheng, X. Fang, Novel structure for high performance UV photodetector based on BiOCl/ZnO hybrid film, Small 13 (2017) 1700156.

[10] S.Q. Guo, X.H. Zhu, H.J. Zhang, B.C. Gu, W. Chen, L. Liu, P.J.J. Alvarez, Improving photocatalytic water treatment through nanocrystal engineering: mesoporous nanosheet-assembled 3D BiOCl hierarchical nanostructures that induce unprecedented large vacancies, Environ. Sci. Technol. 52 (2018) 6872–6880.

[11] S. Wu, W. Sun, J. Sun, Z.D. Hood, S.Z. Yang, L. Sun, P.R.C. Kent, M.F. Chisholm, Surface reorganization leads to enhanced photocatalytic activity in defective BiOCl, Chem. Mater. 30 (2018) 5128–5136.

[12] Y. Liu, W.J. Son, J. Lu, B. Huang, Y. Dai, M.H. Whangbo, Composition dependence of the photocatalytic activities of BiOCl₁₋ₓBrₓ solid solutions under visible light, Chemistry 17 (2011) 9342–9349.

[13] S. Gao, C. Guo, J. Lv, Q. Wang, Y. Zhang, S. Hou, J. Gao, J. Xu, A novel 3D hollow magnetic Fe₃O₄/BiOI heterojunction with enhanced photocatalytic performance for bisphenol A degradation, Chem. Eng. J. 307 (2017) 1055–1065.

[14] F. Dong, Y. Sun, M. Fu, Z. Wu, S.C. Lee, Room temperature synthesis and highly enhanced visible light photocatalytic activity of porous BiOI/BiOCl composites nanoplates microflowers, J. Hazard. Mater. 219-220 (2012) 26–34.

[15] X. Xiao, R. Hao, M. Liang, X. Zuo, J. Nan, L. Li, W. Zhang, One-pot solvothermal synthesis of three-dimensional (3D) BiOI/BiOCl composites with enhanced visible-light photocatalytic activities for the degradation of bisphenol-A, J. Hazard. Mater. 233-234 (2012) 122–130.

[16] W.J. Kim, D. Pradhan, B.K. Min, Y. Sohn, Adsorption/photocatalytic activity and fundamental natures of BiOCl and BiOClₓI₁₋ₓ prepared in water and ethylene glycol environments, and Ag and Au-doping effects, Appl. Catal. B: Environ. 147 (2014) 711–725.

[17] X. Wang, H. Chen, H. Li, G. Mailhot, W. Dong, Preparation and formation mechanism of BiOCl₀.₇₅I₀.₂₅ nanospheres by precipitation method in alcohol-water mixed solvents, J. Colloid. Interf. Sci. 478 (2016) 1–10.

[18] X. Wang, W. Bi, P. Zhai, X. Wang, H. Li, G. Mailhot, W. Dong, Adsorption and photocatalytic degradation of pharmaceuticals by BiOClₓIᵧ nanospheres in aqueous

solution, Appl. Surf. Sci. 360 (2016) 240–251.

[19] H. Wang, L. Zhang, Z. Chen, J. Hu, S. Li, Z. Wang, J. Liu, X. Wang, Semiconductor heterojunction photocatalysts: design, construction, and photocatalytic performances, Chem. Soc. Rev. 43 (2014) 5234–5244.

[20] C. Tan, G. Zhu, M. Hojamberdiev, K. Okada, J. Liang, X. Luo, P. Liu, Y. Liu, Co_3O_4 nanoparticles-loaded BiOCl nanoplates with the dominant {001} facets: efficient photodegradation of organic dyes under visible light, Appl. Catal. B: Environ. 152-153 (2014) 425–436.

[21] D. Feng, Y. Cheng, J. He, L. Zheng, D. Shao, W. Wang, W. Wang, F. Lu, H. Dong, H. Liu, R. Zheng, H. Liu, Enhanced photocatalytic activities of g-C_3N_4 with large specific surface area via a facile one-step synthesis process, Carbon 125 (2017) 454–463.

[22] J. Fu, J. Yu, C. Jiang, B. Cheng, G-C_3N_4-Based heterostructured photocatalysts, Adv. Energy Mater. 8 (2018) 1701503.

[23] W.J. Ong, L.L. Tan, Y.H. Ng, S.T. Yong, S.P. Chai, Graphitic carbon nitride (g-C_3N_4)-based photocatalysts for artificial photosynthesis and environmental remediation: are we a step closer to achieving sustainability? Chem. Rev. 116 (2016) 7159–7329.

[24] W. Liu, L. Qiao, A. Zhu, Y. Liu, J. Pan, Constructing 2D BiOCl/C_3N_4 layered composite with large contact surface for visible-light-driven photocatalytic degradation, Appl. Surf. Sci. 426 (2017) 897–905.

[25] X.J. Wang, Q. Wang, F.T. Li, W.Y. Yang, Y. Zhao, Y.J. Hao, S.J. Liu, Novel BiOCl–C_3N_4 heterojunction photocatalysts: in situ preparation via an ionic-liquid-assisted solvent-thermal route and their visible-light photocatalytic activities, Chem. Eng. J. 234 (2013) 361–371.

[26] C.H.F.P. Charles, T. Campbell, Oxygen vacancies and catalysis on Ceria surfaces, Science 309 (2005) 713–714.

[27] H. Li, J. Li, Z. Ai, F. Jia, L. Zhang, Oxygen vacancy-mediated photocatalysis of BiOCl: reactivity, selectivity, and perspectives, Angew. Chem. Int. Ed. English 57 (2018) 122–138.

[28] Y. Cai, D. Li, J. Sun, M. Chen, Y. Li, Z. Zou, H. Zhang, H. Xu, D. Xia, Synthesis of BiOCl nanosheets with oxygen vacancies for the improved photocatalytic properties, Appl. Surf. Sci. 439 (2018) 697–704.

[29] Z. Zou, H. Xu, D. Li, J. Sun, D. Xia, Facile preparation and photocatalytic activity of oxygen vacancy rich BiOCl with {0 0 1} exposed reactive facets, Appl. Surf. Sci. 463 (2019) 1011–1018.

[30] S. Shi, M.A. Gondal, S.G. Rashid, Q. Qi, A.A. Al-Saadi, Z.H. Yamani, Y. Sui, Q. Xu, K. Shen, Synthesis of g-C_3N_4/BiOCl$_x$Br$_{1-x}$ hybrid photocatalysts and the photoactivity enhancement driven by visible light, Colloids Surf. A Physicochem. Eng. Asp. 461 (2014) 202–211.

[31] Q. Wang, Z. Liu, D. Liu, G. Liu, M. Yang, F. Cui, W. Wang, Ultrathin two-dimensional BiOBr$_x$I$_{1-x}$ solid solution with rich oxygen vacancies for enhanced visible-light-driven photoactivity in environmental remediation, Appl. Catal. B: Environ. 236 (2018) 222–232.

[32] Q. Wang, W. Wang, L. Zhong, D. Liu, X. Cao, F. Cui, Oxygen vacancy-rich 2D/2D BiOCl-g-C_3N_4 ultrathin heterostructure nanosheets for enhanced visible-light-driven photocatalytic activity in environmental remediation, Appl. Catal. B: Environ. 220 (2018) 290–302.

[33] D. Wu, F. Zhang, W. Lou, D. Li, J. Chen, Chemical characterization and toxicity assessment of fine particulate matters emitted from the combustion of petrol and diesel fuels, Sci. Total Environ. 605-606 (2017) 172–179.

[34] F. He, G. Chen, Y. Yu, Y. Zhou, Y. Zheng, S. Hao, The synthesis of condensed C-PDA-g-C_3N_4 composites with superior photocatalytic performance, Chem. Commun. (Camb.) 51 (2015) 6824–6827.

[35] D.H. Yang, G.Q. Gao, Y.W. Zhang, L.S. Zhou, A.W. Xu, W. Chen, Nanosheet-constructed porous BiOCl with dominant {001} facets for superior photosensitized degradation, Nanoscale 4 (2012) 7780–7785.

[36] H.S. Kim, J.B. Cook, H. Lin, J.S. Ko, S.H. Tolbert, V. Ozolins, B. Dunn, Oxygen vacancies enhance pseudocapacitive charge storage properties of MoO3-x, Nat. Mater. 16 (2017) 454–460.

[37] R. Fu, X. Zeng, L. Ma, S. Gao, Q. Wang, Z. Wang, B. Huang, Y. Dai, J. Lu, Enhanced photocatalytic and photoelectrochemical activities of reduced TiO$_{2-x}$/BiOCl heterojunctions, J. Power Sources 312 (2016) 12–22.

[38] L. Wang, G. Zhou, Y. Tian, L. Yan, M. Deng, B. Yang, Z. Kang, H. Sun, Hydroxyl decorated g-C_3N_4 nanoparticles with narrowed bandgap for high efficient photocatalyst design, Appl. Catal. B: Environ. 244 (2019) 262–271.

[39] M. Zhang, C. Lai, B. Li, D. Huang, G. Zeng, P. Xu, L. Qin, S. Liu, X. Liu, H. Yi, M. Li, C. Chu, Z. Chen, Rational design 2D/2D BiOBr/CDs/g-C_3N_4 Z-scheme heterojunction photocatalyst with carbon dots as solid-state electron mediators for enhanced

[40] Y. Li, K. Lv, W. Ho, F. Dong, X. Wu, Y. Xia, Hybridization of rutile TiO$_2$(rTiO$_2$) with g-C_3N_4 quantum dots (CN QDs): an efficient visible-light-driven Z-scheme hybridized photocatalyst, Appl. Catal. B: Environ. 202 (2017) 611–619.

[41] Y. Zeng, X. Liu, C. Liu, L. Wang, Y. Xia, S. Zhang, S. Luo, Y. Pei, Scalable one-step production of porous oxygen-doped g-C_3N_4 nanorods with effective electron separation for excellent visible-light photocatalytic activity, Appl. Catal. B: Environ. 224 (2018) 1–9.

[42] T.L. Kao, H.Y. Tuan, Polymer-mediated metallophilic interactions for gram-scale production, high-yield (approximately 90%) synthesis of ultrathin bismuth nano-wires, Chem. Commun. (Camb.) 53 (2017) 12020–12023.

[43] L. Huang, X. Hu, S. Yuan, H. Li, T. Yan, L. Shi, D. Zhang, Photocatalytic preparation of nanostructured MnO$_2$-(Co$_3$O$_4$)/TiO$_2$hybrids: the formation mechanism and catalytic application in SCR deNO$_x$ reaction, Appl. Catal. B: Environ. 203 (2017) 778–788.

[44] M. Ramadan, A.M. Abdellah, S.G. Mohamed, N.K. Allam, 3D interconnected binder-free electrospun MnO@C nanofibers for supercapacitor devices, Sci. Rep. 8 (2018) 7988.

[45] G. Zhang, Z. Hu, M. Sun, Y. Liu, L. Liu, H. Liu, C.P. Huang, J. Qu, J. Li, Formation of Bi$_2$WO$_6$ bipyramids with vacancy pairs for enhanced solar-driven photoactivity, Adv. Funct. Mater. 25 (2015) 3726–3734.

[46] X. Xue, R. Chen, H. Chen, Y. Hu, Q. Ding, Z. Liu, L. Ma, G. Zhu, W. Zhang, Q. Yu, J. Liu, J. Ma, Z. Jin, Oxygen vacancy engineering promoted photocatalytic Ammonia synthesis on ultrathin two-dimensional bismuth oxybromide nanosheets, Nano Lett. 18 (2018) 7372–7377.

[47] L. Ye, L. Zan, L. Tian, T. Peng, J. Zhang, The {001} facets-dependent high photoactivity of BiOCl nanosheets, Chem. Commun. (Camb.) 47 (2011) 6951–6953.

[48] L. Zhang, W. Wang, D. Jiang, E. Gao, S. Sun, Photoreduction of CO$_2$ on BiOCl nanoplates with the assistance of photoinduced oxygen vacancies, Nano Res. 8 (2014) 821–831.

[49] R. Wang, D. Ren, S. Xia, Y. Zhang, J. Zhao, Photocatalytic degradation of Bisphenol A (BPA) using immobilized TiO$_2$ and UV illumination in a horizontal circulating bed photocatalytic reactor (HCBPR), J. Hazard. Mater. 169 (2009) 926–932.

[50] D. Jing, Y. Pan, D. Li, X. Zhao, B. Bhushan, Effect of surface charge on the nano-friction and its velocity dependence in an electrolyte based on lateral force microscopy, Langmuir 33 (2017) 1792–1798.

[51] S. Li, Z. Feng, Y. Hu, C. Wei, H. Wu, J. Huang, In-situ synthesis and high-efficiency photocatalytic performance of Cu(I)/Cu(II) inorganic coordination polymer quantum sheets, Inorg. Chem. 57 (2018) 13289–13295.

[52] F. Meng, Z. Hong, J. Arndt, M. Li, M. Zhi, F. Yang, N. Wu, Visible light photocatalytic activity of nitrogen-doped La$_2$Ti$_2$O$_7$ nanosheets originating from band gap narrowing, Nano Res. 5 (2012) 213–221.

[53] Y. Li, R. Jin, Y. Xing, J. Li, S. Song, X. Liu, M. Li, R. Jin, Macroscopic foam-like holey ultrathin g-C_3N_4 nanosheets for drastic improvement of visible-light photocatalytic activity, Adv. Energy Mater. 6 (2016) 1601273.

[54] M. Ji, Y. Liu, J. Di, R. Chen, Z. Chen, J. Xia, H. Li, N-CQDs accelerating surface charge transfer of Bi$_4$O$_5$I$_2$ hollow nanotubes with broad spectrum photocatalytic activity, Appl. Catal. B: Environ. 237 (2018) 1033–1043.

[55] D. Zhang, X. Han, T. Dong, X. Guo, C. Song, Z. Zhao, Promoting effect of cyano groups attached on g-C_3N_4 nanosheets towards molecular oxygen activation for visible light-driven aerobic coupling of amines to imines, J. Catal. 366 (2018) 237–244.

[56] Y. Yang, L.C. Yin, Y. Gong, P. Niu, J.Q. Wang, L. Gu, X. Chen, G. Liu, L. Wang, H.M. Cheng, An unusual strong visible-light absorption band in red anatase TiO$_2$ photocatalyst induced by atomic hydrogen-occupied oxygen vacancies, Adv. Mater. 30 (2018) 1704479.

[57] H. Li, L. Zhang, Oxygen vacancy induced selective silver deposition on the {001} facets of BiOCl single-crystalline nanosheets for enhanced Cr(VI) and sodium pentachlorophenate removal under visible light, Nanoscale 6 (2014) 7805–7810.

[58] Y. Fan, W. Ma, D. Han, S. Gan, X. Dong, L. Niu, Convenient recycling of 3D AgX/graphene aerogels (X = Br, Cl) for efficient photocatalytic degradation of water pollutants, Adv. Mater. 27 (2015) 3767–3773.

[59] D. Wu, B. Wang, W. Wang, T. An, G. Li, T.W. Ng, H.Y. Yip, C. Xiong, H.K. Lee, P.K. Wong, Visible-light-driven BiOBr nanosheets for highly facet-dependent photocatalytic inactivation of Escherichia coli, J. Mater. Chem. A Mater. Energy Sustain. 3 (2015) 15148–15155.

visible and NIR photocatalytic activity: kinetics, intermediates, and mechanism insight, J. Catal. 369 (2019) 469–481.